Photocatalytic, Fenton and photo-Fenton degradation of RhB over Z-scheme g-C$_3$N$_4$/LaFeO$_3$ heterojunction photocatalysts

Yongchun Ye[a,b], Hua Yang[a,b,*], Xiangxian Wang[b], Wangjun Feng[b]

[a] State Key Laboratory of Advanced Processing and Recycling of Non-ferrous Metals, Lanzhou University of Technology, Lanzhou 730050, China
[b] School of Science, Lanzhou University of Technology, Lanzhou 730050, China

ARTICLE INFO

ABSTRACT

Z-scheme g-C$_3$N$_4$/LaFeO$_3$ heterojunction photocatalysts were prepared by calcining the uniformly mixed g-C$_3$N$_4$ nanosheets and LaFeO$_3$ nanoparticles at 300 °C for 1 h. The as-prepared g-C$_3$N$_4$/LaFeO$_3$ composites were systematically characterized by XRD, SEM, TEM, XPS, UV–vis DRS, PL spectroscopy, EIS and photocurrent response. It is demonstrated that LaFeO$_3$ nanoparticles (average size: ca. 35 nm) are uniformly assembled onto the surface of g-C$_3$N$_4$ nanosheets through chemical bonding, leading to the formation of g-C$_3$N$_4$/LaFeO$_3$ heterojunctions. The photocatalytic, Fenton and photo-Fenton performances of the samples were investigated by degrading RhB using simulated sunlight as the light source. Compared to bare LaFeO$_3$ and g-C$_3$N$_4$, the g-C$_3$N$_4$/LaFeO$_3$ composites exhibit significantly enhanced photocatalytic and photo-Fenton degradation of the dye, and the maximum activity is observed for the 15%g-C$_3$N$_4$/LaFeO$_3$ composite. Moreover, the photo-Fenton performance of the composites is much higher than the photocatalytic or Fenton performances. The much improved photo-fenton activity is ascribed to the efficient separation of photogenerated electron-hole pairs due to the Z-scheme electron transfer and the synergistic effect between LaFeO$_3$ and g-C$_3$N$_4$. •OH radicals were examined by PL spectroscopy using TPA as a probe molecule, clearly revealing the •OH generation, and moreover, the •OH yield and the dye degradation rate show a similar variation between different cases of the catalysis process. This suggested that •OH is the dominant reactive species causing the dye degradation. The underlying photo-Fenton mechanism of the composites is discussed.

1. Introduction

In recent decades, perovskite-type oxides have been received great attention due to their potential application to deal with the two urgent problems of energy shortage and environmental pollution [1–6]. Perovskite-type oxides have the general formula ABO$_3$ (where A is a rare-earth or alkaline-earth metal element and B is a transition metal element). Due to their unique crystal structures and strong electron-electron interactions, perovskite-type oxides take on a rich variety of physicochemical properties such as catalytic, electrical, magnetic and optical properties. In particular, perovskite-type oxides generally have a relatively narrow bandgap and can efficiently absorb visible light, and moreover they are advantaged by good chemical stability and flexible synthesis. These make perovskite-type oxides attractive as efficiently visible-light-responsive photocatalysts for the degradation of organic pollutants and hydrogen evolution from water splitting. However, the shortcoming of most of the perovskite-type oxides is the high recombination rate of photogenerated electron-hole (e$^-$-h$^+$) pairs. Therefore, it is indispensable to reduce the unfavorable electron-hole

recombination process for enhancing the photocatalytic activity. Numerous strategies have been developed to improve the photocatalytic activity of perovskite-type oxides, such as doping with impurity elements [7,8], construction of heterojunction composites [9,10], decoration with noble metals [11,12] and creation of lattice defects [13,14].

It is well known that, among various wastewater treatment technologies, advanced oxidation processes (AOPs) (such as ozone-based oxidation, electrochemical oxidation, sonochemical oxidation, photocatalytic oxidation and Fenton/photo-Fenton oxidation) have been considered as a high-efficiency and low-cost technology to eliminate organic pollutants [15–20]. As one of the AOPs, Fenton or Fenton-like oxidation technology is particularly attractive, which is mainly based on the generation and utilization of hydroxyl (•OH) radical as the oxidizing agent. The •OH radical is a very powerful oxidizing agent, capable of indiscriminately oxidizing and degrading organic pollutants into harmless inorganic substances. However, the traditional homogeneous Fenton process has some drawbacks including narrow working pH range (pH 2–4), generation of iron sludge, catalyst loss in the effluent

and treatment of secondary pollution from acid or metal ions [21]. Heterogeneous Fenton oxidation has been developed to overcome these problems existing in the homogeneous Fenton process. Moreover, when the heterogeneous Fenton system is irradiated with ultraviolet (UV) or visible light, it brings about a synergistic effect between Fenton oxidation and photocatalysis, and as a result, the photo-Fenton process is much more effective for the oxidative degradation of organic pollutants than Fenton oxidation or photocatalysis. Recently, it was continuously reported that iron-based oxides exhibited great photo-Fenton performance, such as $BaFe_{12}O_{19}/g-C_3N_4$ [22], $Fe_3O_4/C/Cu_2O$ [23], and yolk-shell structured $Fe_3O_4/void/TiO_2$ [24]. More importantly, the formation of heterojunctions in these composites can facilitate the separation of photogenerated electron-hole pairs and induce the synergistic effect between iron-based oxide and another semiconductor. This offers a promising strategy for the further improvement of photo-Fenton performance. Among various perovskite-type oxides, $LaFeO_3$ has been increasingly studied not only due to its photocatalytic activity but also due to its Fenton or photo-Fenton performance [25–29]. Wang et al. [30] immobilized $LaFeO_3$ nanoparticles on carbon spheres to achieve an excellent photo-Fenton performance, much higher than the photocatalytic performance. In our previous study, we found that the photocatalytic performance of $LaFeO_3$ nanoparticles can be significantly enhanced by the decoration of Ag nanoparticles [31].

Graphite-like carbon nitride ($g-C_3N_4$), being a metal-free polymeric semiconductor with relatively small bandgap energy of ca. 2.8 eV, has been shown to be a very promising visible-light-responsive photocatalyst [32]. $g-C_3N_4$ has a sufficiently negative conduction band (CB) edge potential of ca. -1.2 V vs normal hydrogen electrode (NHE), endowing it with a strong photocatalytic reduction capability. Moreover, $g-C_3N_4$ exhibits a good thermal and chemical stability, and can be simply and cheaply prepared by heating carbon- and nitrogen-containing organic precursors such as urea, melamine, cyanamide, dicyandiamide and thiourea. Due to these outstanding properties, $g-C_3N_4$ has been extensively studied for the photocatalytic hydrogen generation from water splitting, reduction of carbon dioxide into useful fuels and removal of environmental pollutants [33–35]. Further, two-dimensional (2D) $g-C_3N_4$ nanosheets have large specific surface area and abundant surface groups, which makes $g-C_3N_4$ nanosheets especially suitable to incorporate with other semiconductors to form heterojunction composite photocatalysts with much enhanced photocatalytic performances [36–42]. Very recently, several research groups reported the construction of $g-C_3N_4/LaFeO_3$ heterojunction composites and found that they showed enhanced photocatalytic degradation of dyes and photocatalytic water splitting into hydrogen [43–47]. However, there is no work concerned with the Fenton or photo-Fenton performances of $g-C_3N_4/LaFeO_3$ heterojunction composites. In this work, we attempted to prepare Z-scheme $g-C_3N_4$ nanosheets/$LaFeO_3$ nanoparticles heterojunction composites via a simple mixing–calcining method, and systematically and comparatively investigate their photocatalytic, Fenton and photo-Fenton performances toward the degradation of rhodamine B (RhB). The underlying photo-Fenton synergistic reaction mechanism was discussed.

2. Experimental

2.1. Preparation of $g-C_3N_4/LaFeO_3$ heterojunction composites

The preparation of $g-C_3N_4/LaFeO_3$ composites was accomplished in three steps. The first step was to prepare $LaFeO_3$ nanoparticles via a polyacrylamide gel route. Stoichiometric amount of $La(NO_3)_3$ (0.0075 mol), $Fe(NO_3)_3$ (0.0075 mol), citric acid (0.0225 mol), glucose (20 g) and acrylamide (0.135 mol) were successively dissolved in 20 mL of dilute nitric acid solution (5 mL HNO_3 + 15 mL deionized water) under continuous stirring using a magnetic bar. The mixture solution was added with deionized water to make a total volume of 100 mL and heated at 80 °C for 4 h, during which time a gel was formed. The gel was

dried in a thermostat drier at 120 °C for 24 h, and then calcinated in a tubular furnace at 500 °C for 3 h, yielding final $LaFeO_3$ nanoparticles. The second step was to prepare $g-C_3N_4$ nanosheets by directly heating melamine in a semiclosed system. 5 g of melamine was loaded in a corundum boat with a cover, and submitted to calcination in a tube furnace at 520 °C for 4 h. The obtained product was ground and collected as $g-C_3N_4$ nanosheets. The third step was to prepare $g-C_3N_4/LaFeO_3$ heterojunction composites. Stoichiometric amount of $g-C_3N_4$ and $LaFeO_3$ were ground together in an agate mortar for 1 h, and then submitted to heat treatment in a tubular furnace at 300 °C for 1 h. The product was collected as final $g-C_3N_4/LaFeO_3$ heterojunction composite. By varying the mass fraction of $g-C_3N_4$ in the composite from 10% to 20%, several composite samples of $10\%g-C_3N_4/LaFeO_3$, $15\%g-C_3N_4/LaFeO_3$ and $20\%g-C_3N_4/LaFeO_3$ were prepared.

2.2. Sample characterization

The crystal phase of the as-prepared samples was determined by x-ray powder diffraction (XRD) using Cu Kα radiation with wavelength of $\lambda = 0.15406$ nm on a D8 Advance x-ray diffractometer. A JSM-6701F field-emission scanning electron microscope (SEM) and a Tecnai G2 20 field-emission transmission electron microscope (TEM) were used to characterize the morphology, microstructure and chemical composition of the samples. The chemical states and composition of the samples were measured by x-ray photoelectron spectroscopy (XPS) on a Thermo Scientific Escalab 250Xi x-ray photoelectron spectrometer. The optical absorption and bandgap energy of the samples was investigated by ultraviolet-visible diffuse reflectance spectroscopy (UV–vis DRS) using $BaSO_4$ as the reference on a TU-1901 double-beam ultraviolet-visible spectrophotometer with an integrating sphere attachment. The photoluminescence (PL) spectra of the samples were measured on a LS-55 fluorescence spectrophotometer with the excitation wavelength of 315 nm.

2.3. Photoelectrochemical measurement

The separation and transfer behavior of photogenerated electrons and holes in the samples was investigated by photocurrent response and electrochemical impedance spectroscopy (EIS) on a CorrTest CST 350 electrochemical workstation. The photoelectrochemical measurements were carried out using a three-electrode cell configuration consisting of a working electrode, a platinum foil counter electrode and a standard calomel electrode (SCE) reference electrode. The working electrode was prepared by mixing together 15 mg of the photocatalyst ($LaFeO_3$ or $15\%g-C_3N_4/LaFeO_3$), 0.75 mg of carbon black and 0.75 mg of polyvinylidene fluoride (PVDF) using 1-methyl-2-pyrrolidinone (NMP) as solvent to form uniform slurry. The slurry was uniformly coated onto fluorine-doped tin oxide (FTO) glass substrate with an effective area of 1×1 cm^2, followed by drying at 60 °C for 5 h in a thermostat drying oven. 0.1 mol L^{-1} Na_2SO_4 aqueous solution was used as the electrolyte. A 200 W xenon lamp was used as the simulated sunlight source. The transient photocurrent response was measured at a bias potential of 0.2 V. The EIS measurement was carried out by the use of the sinusoidal voltage pulse with amplitude of 5 mV over a frequency range of 10^{-2}–10^5 Hz.

2.4. Photocatalytic test

RhB in aqueous solution was chosen as the target organic pollutant to evaluate its photocatalytic degradation, Fenton degradation and photo-Fenton degradation behaviors over $LaFeO_3$ and $g-C_3N_4/LaFeO_3$ samples. A 200 W xenon lamp was used as the simulated sunlight source to evaluate the photocatalytic activity of the samples. In a typical photocatalytic experiment, 50 mg of the photocatalyst and 100 mL of RhB solution with concentration of 10 mg L^{-1} were loaded into the photoreactor. The mixture was magnetically stirred for 30 min in the

dark to establish the adsorption/desorption equilibrium of RhB onto the photocatalyst surface. After that, the mixture was illuminated by a 200 W xenon lamp to initiate the photocatalytic reaction. To avoid the thermal effect on photocatalytic reaction, the photoreactor was cooled with a water-cooling system during the photocatalysis process to maintain the reaction solution at room temperature. At given intervals of 30 min, 2.5 mL of the reaction solution was taken out from the photoreactor to examine the concentration of RhB. The RhB concentration was determined by measuring the absorbance of the solution at a wavelength of λ = 554 nm on a UV–visible spectrophotometer. Before measurement, the photocatalyst particles were removed by centrifugation at 4000 rpm for 10 min. The degradation percentage of the dye is defined as $(C_0 - C_t)/C_0 \times 100\%$, where C_0 is the initial RhB concentration and C_t is the remaining RhB concentration after t min of photocatalysis. As a typical Fenton process for the degradation of RhB, 50 mg of the photocatalyst was loaded in 100 mL of RhB solution, followed by 30 min of magnetic stirring in the dark. Subsequently, 0.5 mL of H_2O_2 was added in the mixture to initiate the Fenton reaction. The whole process of the Fenton experiment was carried out in the dark. In the photo-Fenton process for the RhB degradation, 50 mg of the photocatalyst was loaded in 100 mL of RhB solution and then the mixture was magnetically stirred for 30 min in the dark. After that, the mixture was added with 0.5 mL of H_2O_2 and simultaneously illuminated by a 200 W xenon lamp to initiate the photo-Fenton reaction. During the Fenton and photo-Fenton process, the concentration change of RhB was monitored following the same procedure as described for the photocatalytic process.

2.5. Detection of hydroxyl

During the photocatalysis, Fenton and photo-Fenton process, the production of hydroxyl (•OH) radicals over the photocatalysts was examined by PL spectroscopy using terephthalic acid (TPA) as a probe molecule [48]. A stoichiometric amount of TPA was dissolved in the NaOH aqueous solution with concentration of 1.0 mmol L^{-1} to make a 0.25 mmol L^{-1} TPA solution. To examine the •OH radicals produced during the photocatalysis process, 50 mg of the photocatalyst was loaded in 100 mL of the TPA solution. After magnetically stirred for 30 min in the dark, the mixture was irradiated by a 200 W xenon lamp. After reaction for 120 min, the reaction solution was sampled and centrifuged at 4000 rpm for 10 min to remove the photocatalyst. The upper clear solution in the centrifuge tube was used for the PL measurement at a LS-55 fluorescence spectrophotometer with an excitation wavelength of 315 nm. To examine the •OH radicals produced during the Fenton process, 50 mg of the photocatalyst was loaded in 100 mL of the TPA solution and then the mixture was submitted to magnetic stirring for 30 min in the dark. Subsequently, 0.5 mL of H_2O_2 was added in the mixture to initiate the Fenton reaction. The whole process of the Fenton experiment was carried out in the dark. After 120 min of the Fenton reaction, the reaction solution was sampled for the PL measurement. To examine the •OH radicals produced during the photo-Fenton process, 50 mg of the photocatalyst was loaded in 100 mL of the TPA solution and magnetically stirred for 30 min in the dark. After that, 0.5 mL of H_2O_2 was added in the mixture and simultaneously turn on a 200 W xenon lamp to initiate the photo-Fenton reaction. After Fenton reaction for 120 min, the reaction solution was sampled for the PL measurement.

3. Results and discussion

3.1. XRD analysis

Fig. 1 shows the XRD patterns of the as-prepared LaFeO$_3$, g-C$_3$N$_4$ and g-C$_3$N$_4$/LaFeO$_3$ composites, along with the standard XRD line pattern for LaFeO$_3$ orthorhombic structure (JCPDS#037-1493). It is seen that g-C$_3$N$_4$ displays two typical XRD diffraction peaks at 2θ of
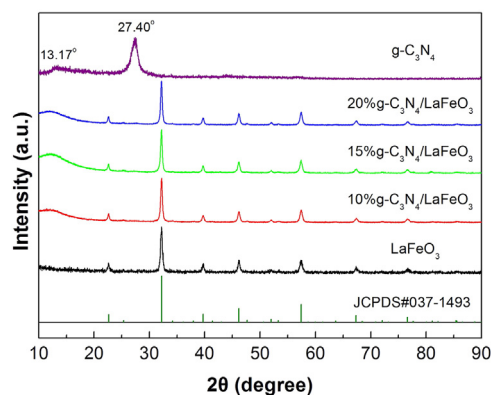

Fig. 1. XRD patterns of the as-prepared LaFeO$_3$, g-C$_3$N$_4$ and g-C$_3$N$_4$/LaFeO$_3$ composites, along with the standard XRD line pattern for LaFeO$_3$ orthorhombic structure (JCPDS#037-1493).

13.17° and 27.40°. The weak diffraction peak at 13.17° can be indexed to the (100) crystal plane of the graphite-like carbon nitride, which arises from the in-plane structural packing motif of tri-s-triazine units. The relatively strong diffraction peak at 27.40° refers to the (002) crystal plane of g-C$_3$N$_4$, which corresponds to the inter-layer stacking of conjugated aromatic system. This indicates the synthesis of g-C$_3$N$_4$ nanosheets using the present experimental method. For LaFeO$_3$, all the diffraction peaks can be perfectly indexed according to the JCPDS#037-1493 standard XRD line pattern, where the dominant diffraction peaks at 2θ = 22.6°, 32.2°, 39.7°, 46.2°, 57.4° and 67.4° correspond to reflections from (101), (121), (220), (202), (240) and (242) crystal planes of the LaFeO$_3$ orthorhombic phase, respectively. For the composites, all the diffraction peaks can be also indexed to the LaFeO$_3$ orthorhombic structure, indicating that there is no structural change in LaFeO$_3$. No obvious diffraction peaks of g-C$_3$N$_4$ are observed in the composites, which is due to several reasons: (1) g-C$_3$N$_4$ accounts for a relatively small fraction of the g-C$_3$N$_4$/LaFeO$_3$ composites, (2) the atomic scattering factor of light elements like C and N is relatively small, and (3) the destruction of long-range-ordered crystal structure for g-C$_3$N$_4$ nanosheets generally results in a low diffraction intensity. In addition, it is seen that the width of the XRD peaks of LaFeO$_3$ in the composites is very similar to that found for bare LaFeO$_3$, indicating that the grain size of LaFeO$_3$ particles undergoes almost no change when they are decorated onto g-C$_3$N$_4$ nanosheets. The average grain size (D) of LaFeO$_3$ particles can be quantitatively evaluated from the XRD peaks using Debye Scherrer formula [49]: $D = k\lambda/(\beta - \beta_0)\cos\theta$, where k is the shape factor ($k = 0.9$), λ is the wavelength of Cu Kα radiation (λ = 0.15406 nm), θ is the diffraction angle, β is the full-width at half maximum (FWHM) of the XRD peaks of LaFeO$_3$, and β_0 is the FWHM of the XRD peaks of a standard reference material (Si). The grain size of LaFeO$_3$ particles estimated from the strongest diffraction peak of (121) is 32 nm.

3.2. SEM and TEM analysis

Fig. 2 shows the SEM image of a typical 15%g-C$_3$N$_4$/LaFeO$_3$ composite, revealing that LaFeO$_3$ particles are uniformly decorated onto two-dimensional g-C$_3$N$_4$ nanosheets. The LaFeO$_3$ particles are seen to present sphere-like or ellipsoid-like morphology and have a size distribution ranging from 20 to 60 nm. The average size of the particles is estimated to be 35 nm, which is very close to (only slightly higher than) their average grain size estimated from XRD data.

TEM investigation was also carried out to further elucidate the morphology and microstructure of g-C$_3$N$_4$/LaFeO$_3$ composites. Fig. 3(a) shows the TEM image of the 15%g-C$_3$N$_4$/LaFeO$_3$ composite. It is demonstrated that g-C$_3$N$_4$ exhibits a typical 2D sheet structure and LaFeO$_3$ particles are shaped like spheres or ellipsoids with an average size of
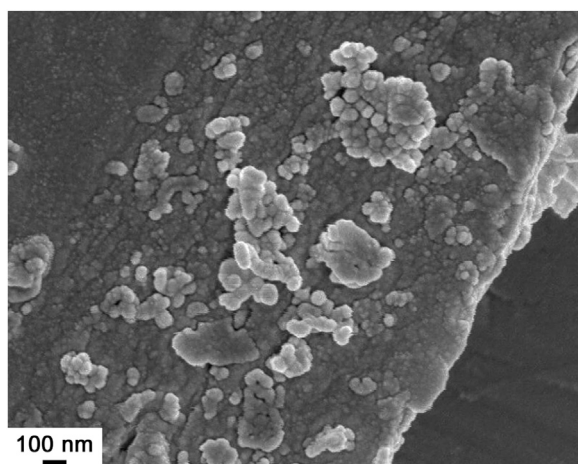
Fig. 2. SEM image of 15%g-C$_3$N$_4$/LaFeO$_3$.

35 nm. The LaFeO$_3$ particles are uniformly decorated onto the surface of g-C$_3$N$_4$ nanosheets almost without aggregation. The morphology and microstructure of the composites observed by TEM is basically in agreement with that observed from the SEM image. Fig. 3(b) shows the high resolution TEM (HRTEM) image of the 15%g-C$_3$N$_4$/LaFeO$_3$ composite, from which one can see that g-C$_3$N$_4$ has a typical amorphous lamellar structure and LaFeO$_3$ exhibits perfect crystal lattice fringes with no internal defects. The lattice fringes with the d-spacing of 0.395 nm correspond to the (101) crystal plane of LaFeO$_3$. The good assembly of LaFeO$_3$ particles onto the surface of g-C$_3$N$_4$ nanosheets leads to the formation of g-C$_3$N$_4$/LaFeO$_3$ heterojunction. Fig. 3(c)

shows the dark-field scanning TEM (DF-STEM) image of the 15%g-C$_3$N$_4$/LaFeO$_3$ composite, and Fig. 3(d)–(h) display the corresponding elemental mapping images of the region marked by yellow rectangle in Fig. 3(c). The bright particles present the uniform elemental distribution of La, Fe and O, and are determined to be LaFeO$_3$. The gray lamellar sheet displays the distribution of C and N elements, and is determined to be g-C$_3$N$_4$. The elemental mapping images further confirm that LaFeO$_3$ particles are uniformly assembled onto g-C$_3$N$_4$ nanosheets to form g-C$_3$N$_4$/LaFeO$_3$ heterojunction. The chemical composition of g-C$_3$N$_4$/LaFeO$_3$ composites is further investigated by the energy-dispersive x-ray spectroscopy (EDS). Fig. 3(i) shows the EDS spectrum of the 15%g-C$_3$N$_4$/LaFeO$_3$ composite, indicating the presence of La, Fe, O, C and N elements in the composite. The observed Cu signal could arise from the Cu microgrid that was used for supporting the sample. It is generally accepted that EDS is sensitive to heavy elements (e.g. La and Fe), but not to light elements (e.g. O, C and N), implying that the relative content of heavy elements can be precisely determined by EDS analysis. The atomic ratio of La/Fe is obtained as 1/1 from the EDS spectrum, which is perfectly consistent with the La/Fe atomic ratio in LaFeO$_3$ phase. However, from the EDS spectrum, it is difficult to determine the actual content of O in the LaFeO$_3$ phase as well as the g-C$_3$N$_4$ content in the g-C$_3$N$_4$/LaFeO$_3$ composite.

3.3. XPS analysis

XPS is an important surface analysis technique that can be used to analyze the chemical states and composition of the samples. The XPS analysis was performed on the 15%g-C$_3$N$_4$/LaFeO$_3$ composite, as shown in Fig. 4. Fig. 4(a) presents the XPS survey scan spectrum, revealing that the elements La, Fe, O, C and N are clearly included in the composite without other impurity elements. The observation of highly intensive C
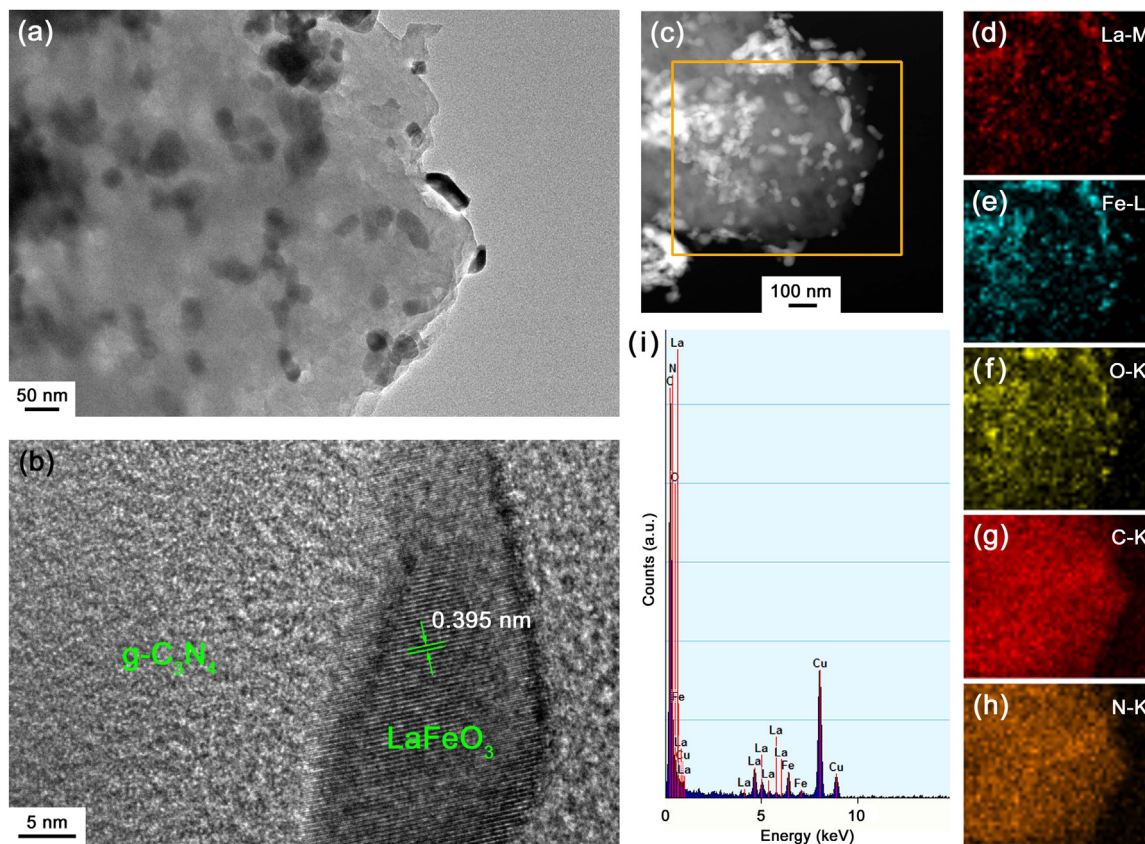

Fig. 3. (a) TEM image of 15%g-C$_3$N$_4$/LaFeO$_3$. (b) HRTEM image of 15%g-C$_3$N$_4$/LaFeO$_3$. (c) DF-STEM image of 15%g-C$_3$N$_4$/LaFeO$_3$. (d)–(h) The corresponding elemental mapping images of the region marked by yellow rectangle in (c). (i) EDS spectrum of 15%g-C$_3$N$_4$/LaFeO$_3$. (For interpretation of the references to color in this figure legend, the reader is referred to the web version of this article.).
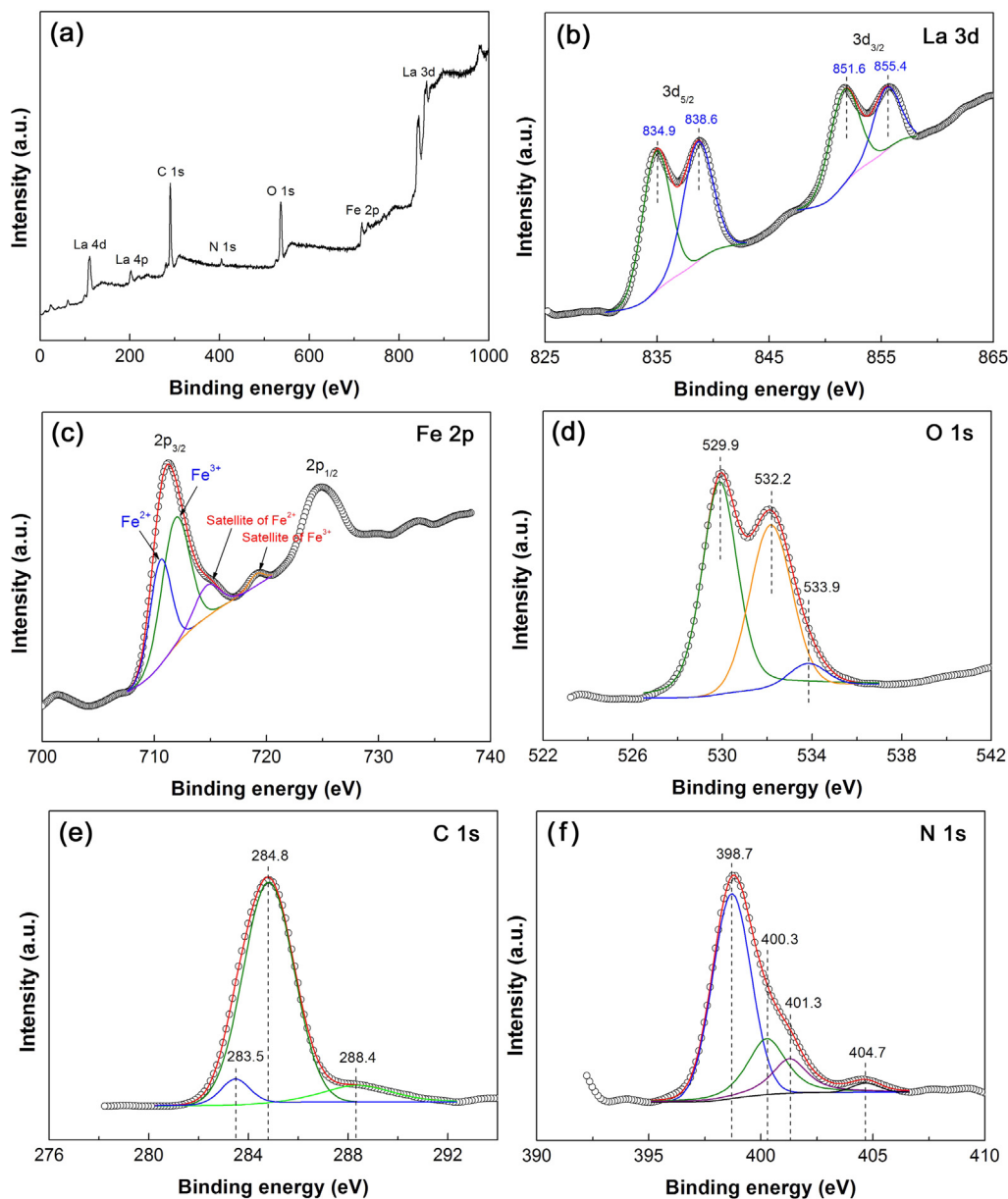
Fig. 4. XPS spectra of 15%g-C_3N_4/LaFeO$_3$. (a) XPS survey scan spectrum; (b) La 3d high-resolution XPS spectrum; (c) Fe 2p high-resolution XPS spectrum; (d) O 1s high-resolution XPS spectrum; (e) C 1s high-resolution XPS spectrum; (f) N 1s high-resolution XPS spectrum.

peak is due to the fact that adventitious carbon (C 1s at 284.8 eV) was used to calibrate the binding energy scale. Fig. 4(b)–(f) show the high-resolution XPS spectra of La 3d, Fe 2p, O 1s, C 1s and N 1s, respectively. The La 3d spectrum presents four peaks, of which the peaks at 834.9 and 851.6 eV are attributed to the binding energies of La $3d_{5/2}$ and La $3d_{3/2}$, respectively, and the peaks at 838.6 and 855.4 eV are characterized as the corresponding satellites of La $3d_{5/2}$ and La $3d_{3/2}$ [50]. The appearance of the satellites on the La 3d levels is due to the spin orbit interaction and electron transfer from the 2p orbital of an oxygen ligand to an empty 4f orbital of lanthanum ions [50]. The La 3d spectrum indicates that lanthanum is in the form of La^{3+} oxidation state. On the Fe 2p spectrum, the Fe $2p_{3/2}$ signal can be deconvoluted into two peaks at 710.5 and 711.8 eV, which are assigned to Fe^{2+} and Fe^{3+}, respectively [51]. Moreover, the Fe^{2+} peak is associated with a satellite at 714.2 eV and the Fe^{3+} peak is associated with a satellite at 719.0 eV. This clearly shows that there exist two oxidation states of iron (Fe^{2+} and Fe^{3+}) in the LaFeO$_3$ particles. The existence of Fe^{2+} oxidation state is usually due to the generation of oxygen vacancies, as confirmed from

the O 1s XPS spectrum. The O 1s signal can be deconvoluted into three peaks at 529.9, 532.2 and 533.9 eV. The binding energy at 529.9 eV is assigned to the crystal lattice oxygen of LaFeO$_3$ [16,17]. The binding energy at 532.2 eV is attributed to chemisorbed hydroxyl species, which is closely associated with oxygen vacancies [17]. The weak peak at binding energy of 533.9 eV is ascribed to surface-adsorbed water molecules [18]. On the C 1s XPS spectrum, three peaks at 283.5, 284.8 and 288.4 eV are observed. The main peak at 284.8 eV is related to sp^2 C–C bonds of adventitious carbon used for the binding energy calibration [52,53]. The peak at 288.4 eV is attributed to the sp^2-hybridized carbon in N-containing aromatic rings (N–C=N) [52,53]. The peak at 283.5 eV could be ascribed to the formation of lanthanum carbide or iron carbide species as a result of the interaction between La/Fe atoms with C atoms. It is noted that the C 1s binding energy for metal carbides is generally positioned at around 283.5 eV [54]. By the peak deconvolution analysis, the N 1s XPS spectrum is seen to consist of four peaks at 398.7, 400.3, 401.3 and 404.7 eV, which correspond to sp^2-hybridized nitrogen in the form of C=N–C, tertiary nitrogen N–(C)$_3$ groups, amino
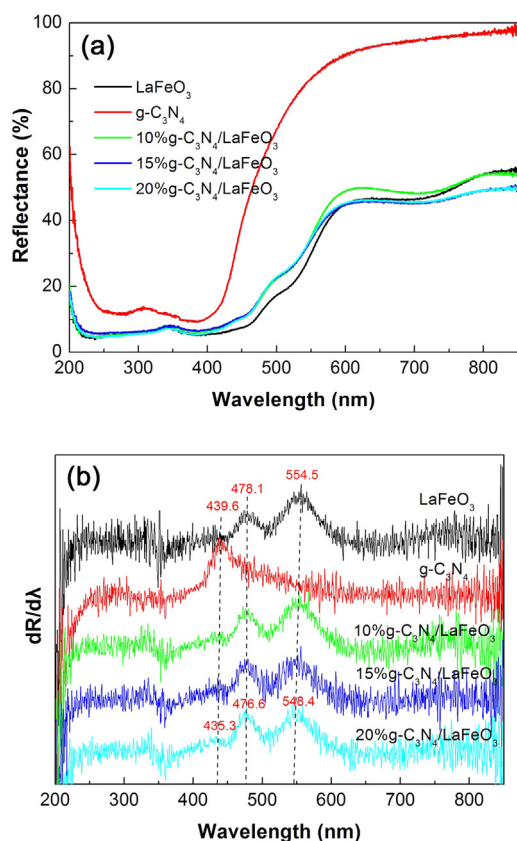
Fig. 5. (a) UV–vis DRS spectra of LaFeO$_3$, g-C$_3$N$_4$ and g-C$_3$N$_4$/LaFeO$_3$ composites. (b) The corresponding first derivative curves of the UV–vis DRS spectra.

functional groups with a hydrogen atom (C–N–H) and π-excitation, respectively [52,53]. This implies a typical characteristic feature of g-C$_3$N$_4$.

3.4. UV–vis DRS spectrum analysis

Fig. 5(a) shows the UV–vis DRS spectra of LaFeO$_3$, g-C$_3$N$_4$ and g-C$_3$N$_4$/LaFeO$_3$ composites, and Fig. 5(b) presents the corresponding first derivative curves of the UV–vis DRS spectra. The absorption edges of the samples associated with the electron transition from the valence band (VB) to the CB can be derived from the peaks on the first derivative spectra. It is seen that g-C$_3$N$_4$ nanosheets exhibit an absorption edge at 439.6 nm, whereas LaFeO$_3$ particles have two obvious absorption edges at 478.1 and 554.5 nm, which are related to the ligand to metal charge transfer (LMCT) and the metal to metal charge transfer (MMCT), respectively [31]. For g-C$_3$N$_4$/LaFeO$_3$ composites, the absorption edges of both LaFeO$_3$ and g-C$_3$N$_4$ exhibit a slight blue shift trend with the increase of g-C$_3$N$_4$ content in the composites. When the g-C$_3$N$_4$ content is increased up to 20%, that is, for the 20%g-C$_3$N$_4$/LaFeO$_3$ composite, the absorption edge of g-C$_3$N$_4$ blue-shifts to 435.3 nm, and the absorption edges of LaFeO$_3$ blue-shift to 476.6 (LMCT) and 548.4 nm (MMCT). From the absorption edges, the bandgap energies of the samples are obtained and given in Table 1. The bandgap energies of both LaFeO$_3$ and g-C$_3$N$_4$ in the composites exhibit a slight increase compared to those of bare LaFeO$_3$ particles and g-C$_3$N$_4$ nanosheets, which could be due to the chemical bonding between LaFeO$_3$ and g-C$_3$N$_4$.

3.5. PL spectrum analysis

To understand the photocatalytic activity of the composites, it is important to reveal the recombination behavior of photogenerated

Table 1
Bandgap energies of LaFeO$_3$, g-C$_3$N$_4$ and g-C$_3$N$_4$/LaFeO$_3$ composites.

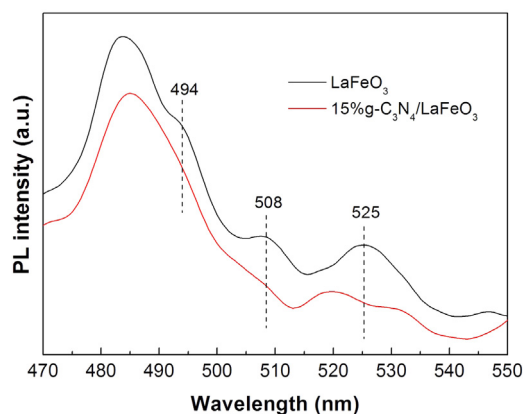| Samples	Bandgap energies of LaFeO$_3$ (eV)		Bandgap energy of g-C$_3$N$_4$ (eV)
	LMCT	MMCT	
LaFeO$_3$	2.59	2.24	–
g-C$_3$N$_4$	–	–	2.82
10%g-C$_3$N$_4$/LaFeO$_3$	2.59	2.25	2.83
15%g-C$_3$N$_4$/LaFeO$_3$	2.60	2.26	2.84
20%g-C$_3$N$_4$/LaFeO$_3$	2.60	2.26	2.85

Fig. 6. PL spectra of LaFeO$_3$ and 15%g-C$_3$N$_4$/LaFeO$_3$.

electron-hole pairs in the composites. PL spectroscopy is an useful technique to evaluate the electron-hole pair recombination. Fig. 6 shows the PL spectra of LaFeO$_3$ and 15%g-C$_3$N$_4$/LaFeO$_3$. Several PL emission peaks are observed at around 494, 508 and 525 nm for bare LaFeO$_3$, and these PL signals arise due to the recombination of photogenerated electrons and holes. In contrast, the PL emission peaks from 15%g-C$_3$N$_4$/LaFeO$_3$ become obviously weakened, implying a decrease in the electron-hole recombination. As a result, more photogenerated electrons and holes in the g-C$_3$N$_4$/LaFeO$_3$ composites are available for participating in the photocatalytic reactions.

3.6. Photoelectrochemical analysis

The separation and transfer behavior of photogenerated electrons and holes in the composites were further investigated by photocurrent response and EIS. Fig. 7(a) shows the transient photocurrent responses of LaFeO$_3$ and 15%g-C$_3$N$_4$/LaFeO$_3$ measured for several on/off cycles of simulated sunlight illumination. When turning on the light, a photocurrent density of ca. 0.04 µA cm^{-2} is observed for bare LaFeO$_3$, and ca. 0.09 µA cm^{-2} for 15%g-C$_3$N$_4$/LaFeO$_3$. After turning off the light, the photocurrent density for both the samples drops to a very low level. This effect appears to be very reproducible when the light source is alternately switched on and off. The observed higher photocurrent density of 15%g-C$_3$N$_4$/LaFeO$_3$ than that of bare LaFeO$_3$ suggests an enhanced electron-hole pair separation in the composite. Fig. 7(b) shows the Nyquist plots of the EIS spectra for LaFeO$_3$ and 15%g-C$_3$N$_4$/LaFeO$_3$, both of which display a semicircle-like shape. It is generally accepted that a smaller diameter of the semicircle means a smaller charge-transfer resistance at the electrode/electrolyte interface. It is obvious that 15%g-C$_3$N$_4$/LaFeO$_3$ has a relatively smaller charge-transfer resistance due to the observation of smaller semicircle diameter as compared to bare LaFeO$_3$. This implies that the composite exhibits more efficient electron-hole separation and faster interface charge transfer under simulated sunlight illumination.

Based on the EIS measurements at different applied potentials (V) in the dark, the flat band potential (V$_{FB}$) of LaFeO$_3$ particles can be also
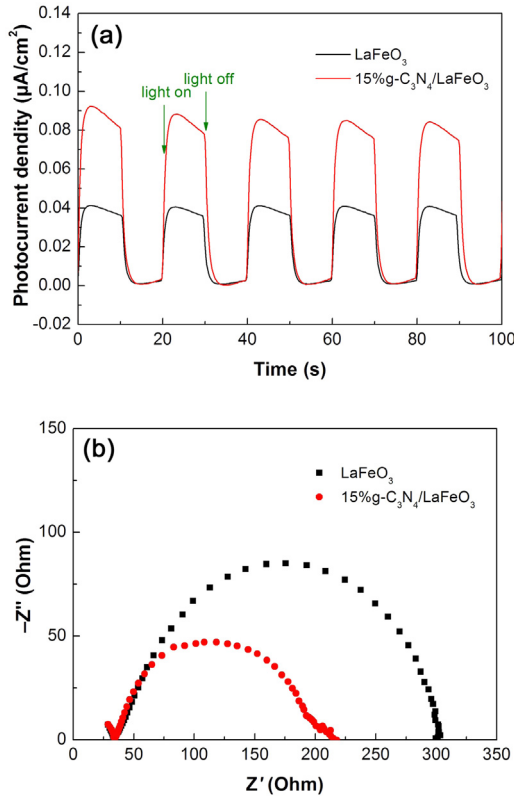
Fig. 7. (a) Transient photocurrent responses of LaFeO$_3$ and 15%g-C$_3$N$_4$/LaFeO$_3$. (b) Nyquist plots of the EIS spectra for LaFeO$_3$ and 15%g-C$_3$N$_4$/LaFeO$_3$.

derived according to the Mott–Schottky equation [55].

$$\frac{1}{C^2} = \left(\frac{2}{e\varepsilon_r\varepsilon_0 N_d A}\right)\left(V - V_{FB} - \frac{kT}{e}\right) \tag{1}$$

where C = space charge capacitance, e = electron charge, ε_r = relative permittivity, ε_0 = vacuum permittivity, N_d = majority carrier density, A = electrode surface area, k = Boltzmann constant, and T = absolute temperature. At room temperature, the temperature-dependent term kT/e can be negligible due to its small value. Thus, the flat band potential can be obtained by extrapolating the linear portion of the Mott–Schottky plot to the V axis. For each applied potential, the space charge capacitance is obtained from the capacitive zone of the Nyquist plots according to the following equation [56]

$$C = \frac{1}{2\pi f |Z_{im}|} \tag{2}$$

where $2\pi f$ is the angular frequency corresponding to the value of the imaginary component of the impedance Z_{im}. For a given frequency, the variation of $1/C^2$ against V is plotted as the Mott–Schottky plot.

Fig. 8 shows the Mott–Schottky plots at different frequencies (3000 and 5000 Hz) for LaFeO$_3$ particles. The two Mott–Schottky plots yield a similar flat band potential of + 1.74 V *vs* SCE. The negative slope of the Mott–Schottky plots implies that LaFeO$_3$ behaves as a p-type semiconductor. Assuming the gap between the flat band potential and the top edge of the VB is negligible for the p-type semiconductor, the VB potential of the p-type semiconductor is roughly equal to its flat band potential. As a result, the VB potential of LaFeO$_3$ is obtained as + 2.40 V *vs* NHE by converting the potential *vs* SCE reference electrode to the potential *vs* NHE according to V(NHE) = V(SCE) + 0.059 pH + 0.242 (here pH = 7) [57]. By considering the MMCT bandgap energy for LaFeO$_3$ ($E_{g,MMCT}$ = 2.24 eV), the CB potential of LaFeO$_3$ is estimated to be + 0.16 V *vs* NHE.
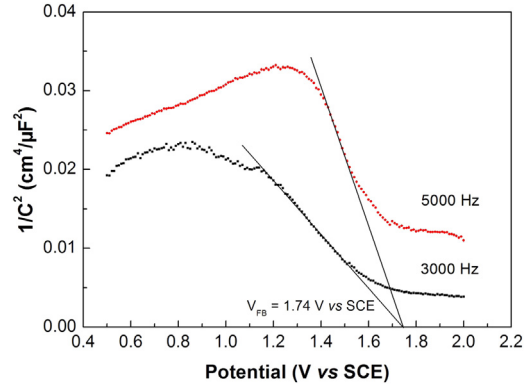

Fig. 8. Mott–Schottky plots of LaFeO$_3$ measured at 3000 and 5000 Hz.

3.7. Photocatalytic, Fenton and photo-Fenton performances

RhB, being one of the famous dyes and widely used as a colorant in paints, textiles and food products, is largely produced in the industrial dye wastewater. RhB is highly water-soluble, chemically stable, carcinogenic and non-biodegradable, and must be artificially removed. Therefore, RhB is generally chosen as a model substrate to evaluate the photocatalyst activity for the pollutant abatement. Fig. 9(a), (c) and (e) show the time-dependent photocatalytic, Fenton and photo-Fenton degradation of RhB over the samples, respectively. Prior to the dye degradation experiments, the dye adsorption was measured in the dark at 30 min of contact time and is obtained to be 4%–10% for all the samples. Moreover, the blank experiments demonstrate that RhB exhibits good stability during the photocatalytic, Fenton and photo-Fenton processes in the absence of the photocatalyst. In all cases of the photocatalytic, Fenton and photo-Fenton experiments, the degradation percentage of the dye after 120 min of reaction is given in Table 2. As seen from Fig. 9(a) and Table 2, the g-C$_3$N$_4$/LaFeO$_3$ composites exhibit a remarkably enhanced photocatalytic activity toward the dye degradation compared to bare LaFeO$_3$ nanoparticles and g-C$_3$N$_4$ nanosheets. With increasing the g-C$_3$N$_4$ content, the optimal photocatalytic activity is observed for the 15%g-C$_3$N$_4$/LaFeO$_3$ composite. We also measured the photocatalytic performance of the composites under UV irradiation and found a similar variation of the photocatalytic performance between the composites, implying that the dye sensitization via visible light absorption do not affect the conclusion of photocatalytic mechanism. From Fig. (c), it is observed that LaFeO$_3$ exhibits an obvious Fenton degradation of RhB, but g-C$_3$N$_4$ has almost no Fenton catalytic activity. The g-C$_3$N$_4$/LaFeO$_3$ composites show a decreased Fenton degradation of the dye compared to bare LaFeO$_3$, which is due to the introduction of g-C$_3$N$_4$ without Fenton catalytic activity, and moreover, the Fenton performance of the composites decreases monotonously with increasing the g-C$_3$N$_4$ content. For the photo-Fenton degradation of RhB as shown in Fig. 9(c), an enhanced photo-Fenton catalytic performance is observed for the g-C$_3$N$_4$/LaFeO$_3$ composites compared to bare LaFeO$_3$ and g-C$_3$N$_4$. Among the composites, the 15%g-C$_3$N$_4$/LaFeO$_3$ composite displays the highest photo-Fenton catalytic activity and the degradation percentage of the dye reaches 97.4% after 120 min of reaction. In addition, it is found that the photo-Fenton performance of the samples (particularly for LaFeO$_3$ and g-C$_3$N$_4$/LaFeO$_3$) is obviously higher than their photocatalytic performance and Fenton performance. This implies that the photo-Fenton catalysis is more efficient for the application in dye wastewater treatment. To further elucidate the catalytic activity of the samples in every case, the degradation kinetics of the dye is investigated. Fig. 9(b), (d) and (f) show the plots of Ln(C_t/C_0) *vs* irradiation time t for the photocatalytic, Fenton and photo-Fenton degradation of RhB, respectively. It is seen that the dye degradation process conforms well to the first-order kinetic equation Ln(C_t/C_0) = $-k_{app}t$, where k_{app} is the apparent first-
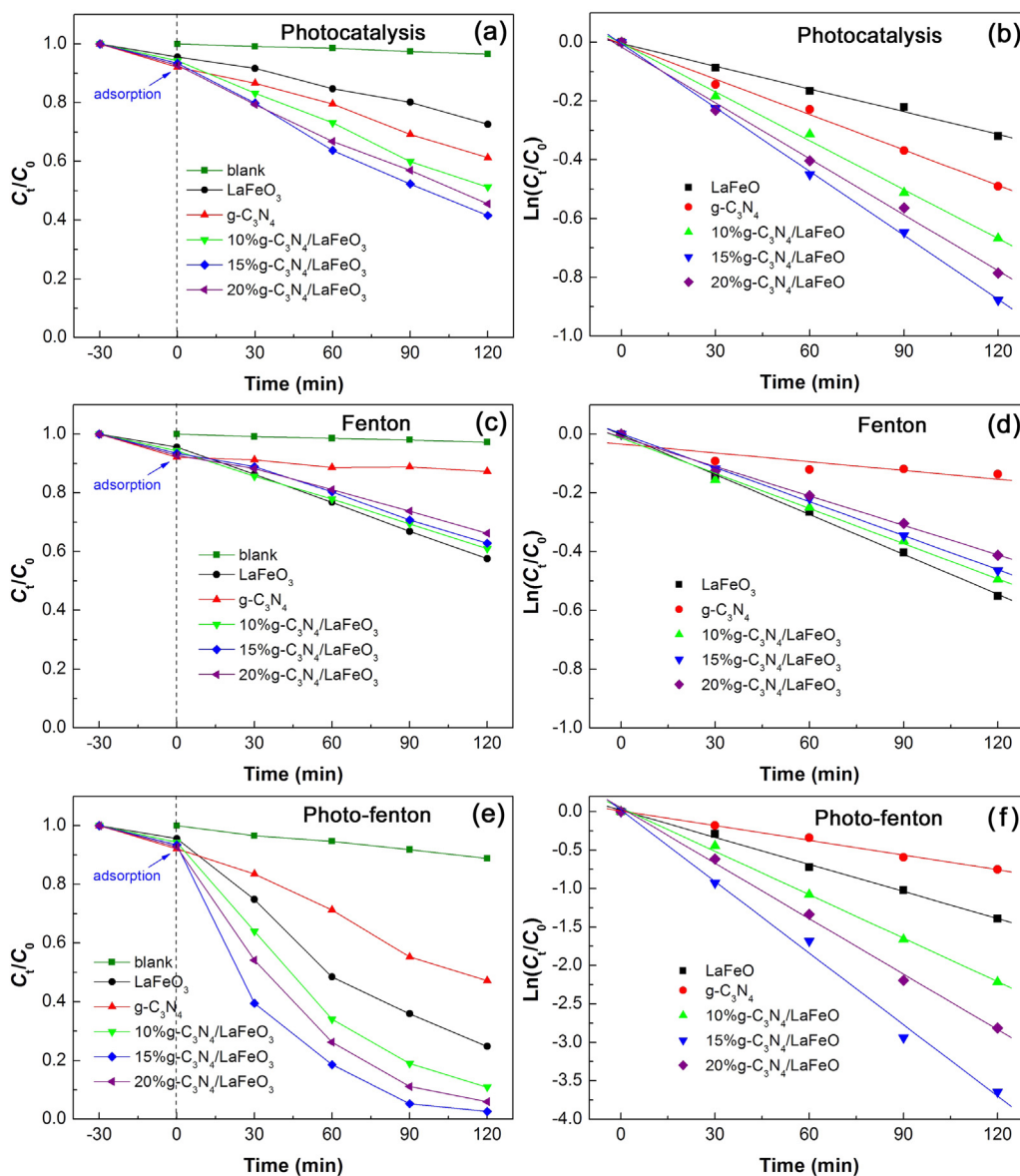
Fig. 9. (a), (c) and (e) Time-dependent photocatalytic, Fenton and photo-Fenton degradation of RhB over the samples, respectively. (b), (d) and (f) Plots of Ln(C_t/C_0) vs irradiation time t for the photocatalytic, Fenton and photo-Fenton degradation of RhB, respectively.

order reaction rate constant (min^{-1}) [58]. From the slope of the regression lines, The rate constant k_{app} is obtained and given in Table 2. Based on the rate constant, it is concluded that the 15%g-C$_3$N$_4$/LaFeO$_3$ composite has a photocatalytic activity about 2.8 and 1.8 times higher than those of bare LaFeO$_3$ and g-C$_3$N$_4$, respectively, and moreover the composite has a photo-Fenton catalytic activity about 2.6 and 4.9 times higher than those of bare LaFeO$_3$ and g-C$_3$N$_4$ respectively.

The reusability is one of the important factors for the practical application of the catalyst in dye wastewater treatment. In the present study, the reusability of the 15%g-C$_3$N$_4$/LaFeO$_3$ composite for the photocatalytic, Fenton and photo-Fenton degradation of RhB was investigated by the recycling experiment. After the completion of the first cycle of the catalysis, the photocatalyst was collected by centrifugation, washed with deionized water and then dried in a thermostat drying
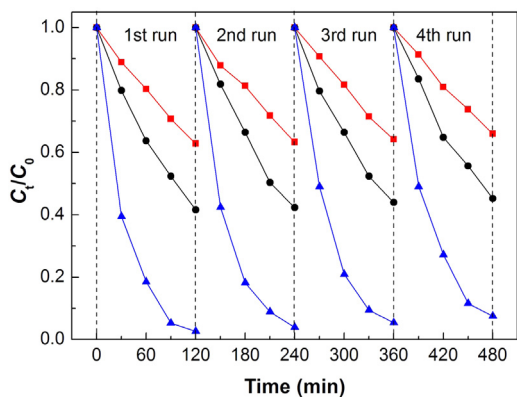
Table 2
Degradation percentage of the dye after 120 min of reaction and the apparent first-order reaction rate constant for the photocatalytic, Fenton and photo-Fenton processes over the samples.

Samples	Photocatalysis		Fenton		Photo-Fenton	
	Degradation (%)	K_{app} (min^{-1})	Degradation (%)	K_{app} (min^{-1})	Degradation (%)	K_{app} (min^{-1})
LaFeO$_3$	27.4	0.00258	42.4	0.00453	75.2	0.01174
g-C$_3$N$_4$	38.8	0.00402	12.7	0.00099	52.8	0.00638
10%g-C$_3$N$_4$/LaFeO$_3$	48.7	0.00555	39.1	0.00400	89.1	0.01883
15%g-C$_3$N$_4$/LaFeO$_3$	58.4	0.00726	37.2	0.00386	97.4	0.03100
20%g-C$_3$N$_4$/LaFeO$_3$	54.4	0.00635	33.8	0.00334	94.0	0.02403

Fig. 10. Photocatalytic (black plot), Fenton (red plot) and photo-Fenton (blue plot) degradation of RhB over 15%g-C$_3$N$_4$/LaFeO$_3$ repeatedly used for four times. (For interpretation of the references to color in this figure legend, the reader is referred to the web version of this article.).

oven at 60 °C for 5 h. The recovered photocatalyst was used for the next cycle of the catalytic degradation of the dye. This process was repeated for three times. Fig. 10 shows the photocatalytic (black plot), Fenton (red plot) and photo-Fenton (blue plot) degradation of RhB during four catalytic cycles over the 15%g-C$_3$N$_4$/LaFeO$_3$ composite. At the 4th cycle of the photocatalysis, Fenton catalysis and photo-Fenton catalysis, the dye degradation after 120 min of reaction reaches 54.8%, 34.1% and 92.4%, respectively, compared to 58.4%, 37.2% and 97.4% at the 1st cycle of the corresponding catalytic degradation of the dye. This implies that the composite retains a good catalytic stability after recycling for four times.

The morphology, microstructure and crystal structure of the 15%g-C$_3$N$_4$/LaFeO$_3$ composite after four times of photocatalytic recycling were investigated by TEM and XRD. The TEM image shown in Fig. 11(a) reveals that LaFeO$_3$ particles are uniformly decorated onto two-dimensional g-C$_3$N$_4$ nanosheets. The HRTEM image given in Fig. 11(b) demonstrates that LaFeO$_3$ displays perfect crystal lattice fringes with the d-spacing of 0.279 nm, which correspond to the (121) facet of LaFeO$_3$. The XRD pattern presented in Fig. 11(c) shows that all the diffraction peaks can be perfectly indexed according to the LaFeO$_3$ orthorhombic phase (JCPDS#037-1493). The TEM and XRD investigation reveals the good assembly of LaFeO$_3$ particles onto g-C$_3$N$_4$ nanosheets and the microstructure and crystal structure of the composite undergoes almost no change after four times of photocatalytic recycling.

3.8. •OH radical analysis

In most of the photocatalysts including LaFeO$_3$, •OH radicals have been shown to be the dominant reactive species causing the dye degradation. In the present study, the production of •OH during the photocatalysis, Fenton and photo-Fenton process was investigated by PL spectroscopy using TPA as a probe molecule. It is noted that TPA can react with •OH to produce 2-hydroxyterephthalic acid (TAOH), which is an excellent fluorescent compound with a characteristic photoluminescence at around 429 nm. The intensity of the PL peak is related to the amount of produced •OH radicals. Fig. 12(a) shows the PL spectra of the TPA solution after 120 min of the photocatalysis, Fenton or photo-Fenton reaction over the samples, along with the blank experiment result. In all cases of the catalysis reaction, the TPA solution shows an obvious PL signal centered around 429 nm, whereas no PL signal is observed for blank TPA solution. This indicates that •OH radicals are
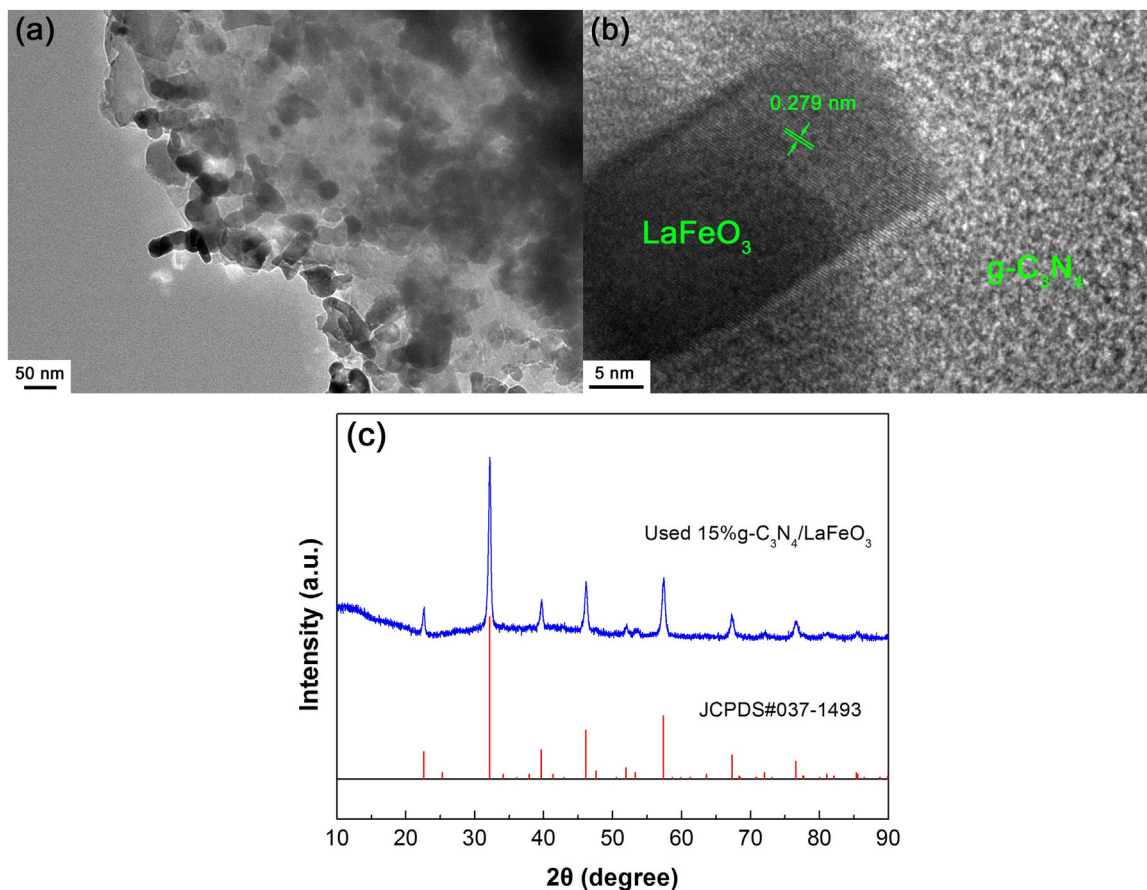

Fig. 11. TEM image (a), HRTEM image (b) and XRD pattern (c) of 15%g-C$_3$N$_4$/LaFeO$_3$ after four times of photocatalytic recycling.
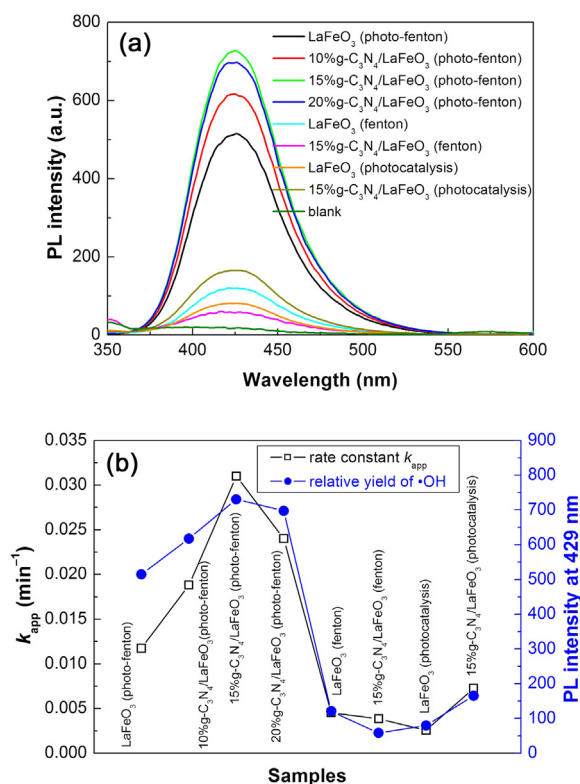
Fig. 12. (a) PL spectra of the TPA solution after 120 min of the photocatalysis, Fenton or photo-Fenton reaction over the samples, along with the blank experiment result. (b) Variation of the PL peak intensity and the rate constant k_{app} between different cases of the catalysis process.

produced in all cases of the catalysis process. The highest intensity of the PL peak is observed for the photo-Fenton reaction over the 15%g-C_3N_4/LaFeO$_3$ composite, implying the production of the largest amount of •OH radicals. In order to clearly elucidate the correlation of the •OH yield with the catalytic performance, the variation of the PL peak intensity (i.e. the •OH yield) and the rate constant k_{app} between different cases of the catalysis process are plotted in Fig. 12(b). It is seen that the variation of the rate constant basically agrees with the variation of the PL peak intensity, indicating that the catalytic performance is highly

dependent on the •OH yield and hence •OH radicals are confirmed to be the dominant reactive species responsible for the dye degradation. The existence of superoxide (•O_2^-) can not be excluded in the present catalytic systems; however, •O_2^- radicals play only a minor or secondary role in the dye degradation [31].

3.9. Photo-Fenton mechanism

A possible photo-Fenton mechanism is proposed to elucidate the enhanced catalytic activity of the g-C_3N_4/LaFeO$_3$ heterojunction composites for the dye degradation, as shown in Fig. 13. The E_g of LaFeO$_3$ and g-C_3N_4 is 2.24 eV (here considering the typical MMCT E_g for LaFeO$_3$) and 2.82 eV, respectively. The CB/VB potentials of LaFeO$_3$ and g-C_3N_4 are obtained as + 0.16/+ 2.40 and − 1.18/+ 1.64 V vs NHE, respectively [31]. Due to their unique band edge positions, LaFeO$_3$ is expected to incorporate with g-C_3N_4 to form Z-scheme g-C_3N_4/LaFeO$_3$ heterojunction photocatalysts. Under irradiation of simulated sunlight, the photogenerated electrons in the CB of LaFeO$_3$ will transfer to g-C_3N_4 and recombine with the photogenerated holes in the VB of g-C_3N_4. The internal electric field at the interface of the g-C_3N_4/LaFeO$_3$ heterojunction acts as the driving force for the Z-scheme electron transfer, and moreover the formed chemical bonds between g-C_3N_4 and LaFeO$_3$ like C–La/Fe bonds as revealed by XPS and UV–vis DRS are also conducive to the electron transfer. Due to the Z-scheme electron transfer, more photogenerated holes in the VB of LaFeO$_3$ and photogenerated electrons in the CB of g-C_3N_4 are available for participating the photocatalytic reactions. As a result, the g-C_3N_4/LaFeO$_3$ composites exhibit enhanced photocatalytic performance compared to bare LaFeO$_3$ and g-C_3N_4. It is noted that the photogenerated holes in the VB of LaFeO$_3$ do not oxidize the dye molecules directly, but react with OH$^-$ species to produce highly oxidative •OH radicals, which are confirmed to be the dominant reactive species causing the dye degradation. This •OH generation process is feasible from a thermodynamic point of view since the VB potential of LaFeO$_3$ (+ 2.40 V vs NHE) is positive to the redox potential of OH$^-$/•OH (+ 1.99 V vs NHE) [52]. The CB potential of g-C_3N_4 (− 1.18 V vs NHE) is more negative than the redox potential of O_2/•O_2^- (− 0.33 V vs NHE) [48], implying that the photogenerated electrons in the CB of g-C_3N_4 can react with O_2 dissolved in the reaction solution to produce •O_2^- radicals. However, compared to •OH radicals, the effect of •O_2^- radicals on the dye degradation is very small and can be negligible. When adding H_2O_2 to the reaction solution, the photo-Fenton catalytic process is proceeded. Another important amount of •OH radicals are produced via the photo-Fenton process, i.e., the
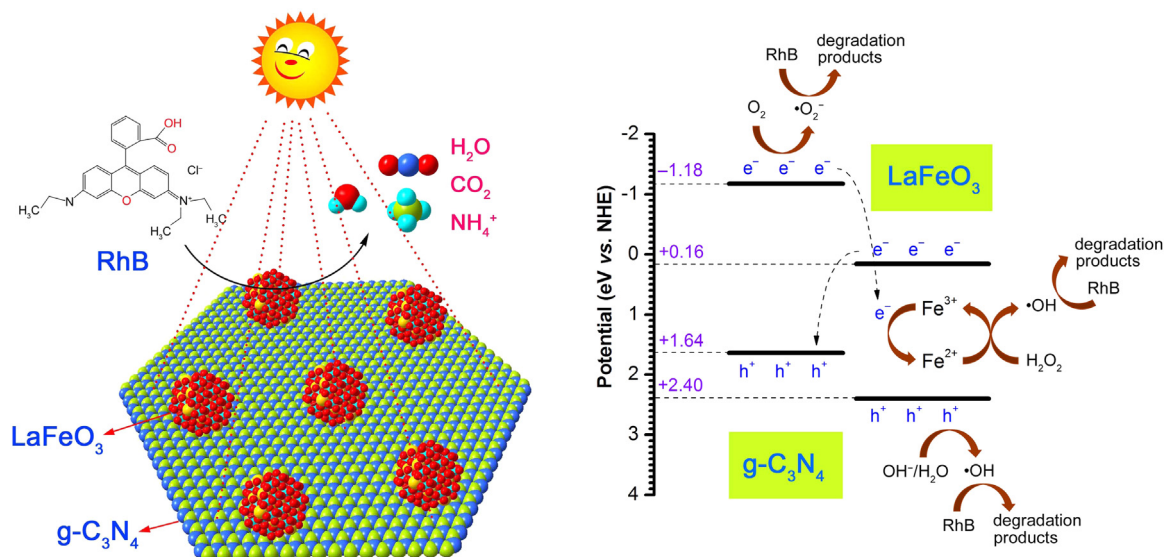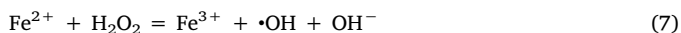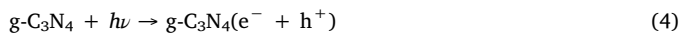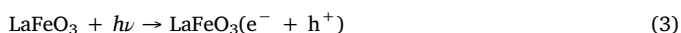

Fig. 13. Schematic illustration of the photo-Fenton mechanism for g-C_3N_4/LaFeO$_3$ composites.

reaction of Fe^{2+} with H_2O_2 [23,24]. Simultaneously, the photo-generated electrons in the CB of g-C_3N_4 cause the reduction of Fe^{3+} to Fe^{2+}, making the photo-Fenton process proceed continuously. Benefitting from this electron reduction, the photo-Fenton process for the g-C_3N_4/LaFeO$_3$ composites is more efficient than that for bare LaFeO$_3$. Additional •OH radicals can be also generated by the direct UV photolysis of H_2O_2. However, this is only a secondary pathway for the •OH generation because in the present study simulated sunlight was used as the light source, which contains only a small fraction of UV light. The main reactions involved in the photo-Fenton process can be briefly described by Eqs. (3)–(9). As seen from the above discussion, the creation of g-C_3N_4/LaFeO$_3$ heterojunctions is crucial for achieving excellent photocatalytic or photo-Fenton performance of the composites. An appropriate proportion of g-C_3N_4 and LaFeO$_3$ is required for the creation of the maximum amount of g-C_3N_4/LaFeO$_3$ heterojunctions in the composites. The optimum content of g-C_3N_4 in the composites is observed to be 15%, and as a consequence, the 15%g-C_3N_4/LaFeO$_3$ composite exhibits the highest photocatalytic or photo-Fenton activity toward the dye degradation.

$$LaFeO_3 + h\nu \rightarrow LaFeO_3(e^- + h^+) \tag{3}$$

$$g\text{-}C_3N_4 + h\nu \rightarrow g\text{-}C_3N_4(e^- + h^+) \tag{4}$$

$$h^+(LaFeO_3) + OH^- \rightarrow \text{•OH} \tag{5}$$

$$e^-(g\text{-}C_3N_4) + O_2 \rightarrow \text{•}O_2^- \tag{6}$$

$$Fe^{2+} + H_2O_2 = Fe^{3+} + \text{•OH} + OH^- \tag{7}$$

$$Fe^{3+} + e^-(g\text{-}C_3N_4) = Fe^{2+} \tag{8}$$

$$H_2O_2 + h\nu \rightarrow 2\text{•OH} \tag{9}$$

4. Conclusions

LaFeO$_3$ nanoparticles with average size of ca. 35 nm were integrated with g-C_3N_4 nanosheets to form Z-scheme g-C_3N_4/LaFeO$_3$ heterojunction photocatalysts via a simple mixing–calcining method. The g-C_3N_4/LaFeO$_3$ composites demonstrate an efficient photogenerated electron-hole pair separation due to the Z-scheme electron transfer. As a result, the composites exhibit enhanced photocatalytic and photo-Fenton performances for the RhB degradation compared to bare LaFeO$_3$ and g-C_3N_4. The maximum photocatalytic or photo-Fenton activity is observed for the 15%g-C_3N_4/LaFeO$_3$ composite. Moreover, the synergistic effect between LaFeO$_3$ and g-C_3N_4 makes the photo-Fenton performance of the composites much higher than the photocatalytic performance. •OH radicals are found to be generated in the photocatalytic, Fenton and photo-Fenton processes over the samples. The yield of •OH radicals varies consistently with the dye degradation rate between different cases of the catalysis process. It is concluded from the experimental results that •OH is the dominant reactive species responsible for the dye degradation.

Acknowledgements

References

[1] P. Kanhere, Z. Chen, Molecules 19 (2014) 19995–20022.
[2] X.Y. Wu, X.Y. Wang, J. Li, G.K. Zhang, J. Mater. Chem. A 5 (2017) 23822–23830.
[3] Y.X. Yan, H. Yang, X.X. Zhao, H.M. Zhang, J.L. Jiang, J. Electron. Mater. ⟨http://dx.doi.org/dx.doi.org/10.1007/s11664-018-6183-z⟩.
[4] N. Labhasetwar, G. Saravanan, S.K. Megarajan, N. Manwar, R. Khobragade, P. Doggali, F. Grasset, Sci. Technol. Adv. Mater. 16 (2015) 36002.
[5] M. Zhou, H. Yang, T. Xian, R.S. Li, H.M. Zhang, X.X. Wang, J. Hazard. Mater. 289 (2015) 149–157.
[6] J. Shi, L. Guo, Prog. Nat. Sci. Mater. Int. 22 (2012) 592–615.
[7] G. Iervolino, V. Vaiano, D. Sannino, L. Rizzo, V. Palma, Appl. Catal. B-Environ. 207 (2017) 182–194.
[8] X.Q. Sun, Y.H. Xie, F.F. Wu, H.M. Chen, M.L. Lv, S. Ni, G. Liu, X.X. Xu, Inorg. Chem. 54 (2015) 7445–7453.
[9] Y. Wu, Y.L. Wei, Q.Y. Guo, H. Xu, L. Gu, F.Y. Huang, D. Luo, Y.F. Huang, L.Q. Fan, J.H. Wu, Sol. Energy Mater. Sol. Cells 176 (2018) 230–238.
[10] K. Nakamura, H. Mashiko, K. Yoshimatsu, A. Ohtomo, Appl. Phys. Lett. 108 (2016) 211605.
[11] S.D. Li, Y. Zhao, C.Y. Wang, D.D. Li, K. Gao, Mater. Lett. 170 (2016) 122–125.
[12] F. Wang, H. Yang, H.M. Zhang, J.L. Jiang, J. Mater. Sci. -Mater. El 29 (2018) 1304–1316.
[13] H.Q. Tan, Z. Zhao, W.B. Zhu, E.N. Coker, B.S. Li, M. Zheng, W.X. Yu, H.Y. Fan, Z.C. Sun, ACS Appl. Mater. Inter. 6 (2014) 19184–19190.
[14] L.J. Di, H. Yang, T. Xian, X.J. Chen, Materials 10 (2017) 1118.
[15] H.W. Wang, X.Y. Li, Z.P. Hao, Y.J. Sun, Y.N. Wang, W.H. Li, Y.F. Tsang, J. Environ. Manag. 191 (2017) 244–251.
[16] F.C. Moreira, R.A.R. Boaventura, E. Brillas, V.J.P. Vilar, Appl. Catal. B-Environ. 202 (2017) 217–261.
[17] R. Behling, G. Chatel, S. Valange, Ultrason. Sonochem. 36 (2017) 27–35.
[18] C.X. Zheng, H. Yang, Z.M. Cui, H.M. Zhang, X.X. Wang, Nanoscale Res. Lett. 12 (2017) 608.
[19] T. Fan, Y.G. Li, H. Zhang, Ind. Eng. Chem. Res. 56 (2017) 11684–11696.
[20] M.J. Lima, C.G. Silva, A.M.T. Silva, J.C.B. Lopes, M.M. Dias, J.L. Faria, Chem. Eng. J. 310 (2017) 342–351.
[21] J. Herney-Ramirez, M.A. Vicente, L.M. Madeira, Appl. Catal. B-Environ. 98 (2010) 10–26.
[22] H. Wang, Y. Xu, L. Jing, S. Huang, Y. Zhao, M. He, H. Xu, H. Li, J. Alloy. Compd. 710 (2017) 510–518.
[23] F. Chai, K. Li, C. Song, X. Guo, J. Colloid Interface Sci. 475 (2016) 119–125.
[24] D. Du, W. Shi, L. Wang, J. Zhang, Appl. Catal. B-Environ. 200 (2017) 484–492.
[25] G. Iervolino, V. Vaiano, D. Sannino, L. Rizzo, P. Ciambelli, Int. J. Hydrog. Energ. 41 (2016) 959–966.
[26] H.F. Shen, T. Xue, Y.M. Wang, G.Z. Cao, Y.J. Lu, G.L. Fang, Mater. Res. Bull. 84 (2016) 15–24.
[27] X.C. Hao, Y.C. Zhang, Mater. Lett. 197 (2017) 120–122.
[28] Y.L. Nie, L.L. Zhang, Y.Y. Li, C. Hu, J. Hazard. Mater. 294 (2015) 195–200.
[29] V. Vaiano, G. Iervolino, D. Sannino, L. Rizzo, G. Sarno, P. Ciambelli, L.A. Isupova, J. Environ. Eng. 141 (2015) 04015038.
[30] K. Wang, H. Niu, J. Chen, J. Song, C. Mao, S. Zhang, Y. Gao, Appl. Surf. Sci. 404 (2017) 138–145.
[31] Y.C. Ye, H. Yang, R.S. Li, X.X. Wang, J. Sol-Gel Sci. Technol. 82 (2017) 509–518.
[32] X. Wang, K. Maeda, A. Thomas, K. Takanabe, G. Xin, J.M. Carlsson, K. Domen, M. Antonietti, Nat. Mater. 8 (2009) 76–80.
[33] S. Patnaik, S. Martha, S. Acharya, K.M. Parida, Inorg. Chem. Front. 3 (2016) 336–347.
[34] F.L. Yang, F.F. Xia, J. Hu, C.Z. Zheng, J.H. Sun, H.B. Yi, RSC Adv. 8 (2018) 1899–1904.
[35] J. Wen, J. Xie, X. Chen, X. Li, Appl. Surf. Sci. 391 (2017) 72–123.
[36] Z.M. Cui, H. Yang, X.X. Zhao, Mater. Sci. Eng. B 229 (2018) 160–172.
[37] J. Li, Y.C. Yin, E.Z. Liu, Y.N. Ma, J. Wan, J. Fan, X.Y. Hu, J. Hazard. Mater. 321 (2017) 183–192.
[38] L. Zhou, W. Zhang, L. Chen, H. Deng, J. Colloid Interface Sci. 487 (2017) 410–417.
[39] Z.X. Sun, H.Q. Wang, Z.B.A. Wu, L.Z. Wang, Catal. Today 300 (2018) 160–172.
[40] S. Thaweesak, M. Lyu, P. Peerakiatkhajohn, T. Butburee, B. Luo, H. Chen, L. Wang, Appl. Catal. B-Environ. 202 (2017) 184–190.
[41] Y. Wu, H. Wang, Y.M. Sun, T. Xiao, W.G. Tu, X.Z. Yuan, G.M. Zeng, S.Z. Li, J.W. Chew, Appl. Catal. B-Environ. 227 (2018) 530–540.
[42] H. Wang, X.Z. Yuan, Y. Wu, G.M. Zeng, X.H. Chen, L.J. Leng, H. Li, Appl. Catal. B-Environ. 174 (2015) 445–454.
[43] Q. Liang, J. Jin, C. Liu, S. Xu, Z. Li, J. Alloy. Compd. 709 (2017) 542–548.
[44] K. Xu, H. Xu, G. Feng, J. Feng, New J. Chem. 41 (2017) 14602–14609.
[45] S. Acharya, S. Mansingh, K.M. Parida, Inorg. Chem. Front. 4 (2017) 1022–1032.
[46] K. Xu, J. Feng, RSC Adv. 7 (2017) 45369–45376.
[47] Y. Wu, H. Wang, W. Tu, Y. Liu, Y.Z. Tan, X. Yuan, J.W. Chew, J. Hazard. Mater. 347 (2018) 412–422.
[48] X. Zhao, H. Yang, Z. Cui, R. Li, W. Feng, Mater. Technol. 32 (2017) 870–880.
[49] M.P. Klug, L.E. Alexander, X-Ray Diffraction Procedure for Polycrystalline and Amorphous Materials, Wiley, New York, 1974, p. 634.
[50] R.J. Signorclli, R.G. Hayes, Phys. Rev. B 8 (1973) 81–86.
[51] T. Yamashita, P. Hayes, Appl. Surf. Sci. 254 (2008) 2441–2449.
[52] G.Q. Tan, L.N. She, T. Liu, C. Xu, H.J. Ren, A. Xia, Appl. Catal. B-Environ. 207 (2017) 120–133.
[53] K.L. He, J. Xie, X.Y. Luo, J.Q. Wen, S. Ma, X. Li, Y.P. Fang, X.C. Zhang, Chin. J. Catal. 38 (2017) 240–252.
[54] Q.D. Ling, S. Li, E.T. Kang, K.G. Neoh, B. Liu, W. Huang, Appl. Surf. Sci. 199 (2002) 74–82.
[55] A. Fattah-alhosseini, Arab. J. Chem. 9 (2016) S1342–S1348.
[56] F. Cardon, W.P. Gomes, J. Phys. D-Appl. Phys. 11 (1978) L63–L67.
[57] F. Wang, H. Yang, Y.C. Zhang, Mater. Sci. Semicond. Proc. 73 (2018) 58–66.
[58] I.K. Konstantinou, T.A. Albanis, Appl. Catal. B-Environ. 49 (2004) 1–14.